RESEARCH ARTICLE

OPEN ACCESS   Check for updates

Prediction and Simulation for Land Use and Land Cover Change of Paddy Field Influence by Salinization in Coastal Demak Regency

Tommy Andryan Tivianton[ab], Baba Barus[a], Moh Yanuar Jarwadi Purwanto[a], Syaiful Anwar[a], Widiatmaka[a]

[a] Natural Resources and Environmental Management, Graduate School, IPB University, IPB Baranangsiang Campus, Bogor, 16129, Indonesia
[b] Department of Environmental Geography, Faculty of Geography, Universitas Gadjah Mada, Yogyakarta, 55281, Indonesia

ABSTRACT

The extent of coastal rice paddy agricultural land is vulnerable to land use and land cover (LULC) changes to non-agricultural uses due to land degradation, one of which is caused by salinity. This study aims to detect and project LULC changes up to 2031, particularly in coastal rice paddy areas affected by salinity, by comparing LULC in 2017, 2019, and 2021. Sentinel-2 Imagery is used for LULC classification, with recordings selected during the generative phase of rice growth to obtain the most optimal rice paddy area. There are six LULC classifications: water, wetland, low-medium-high vegetation cover, and built-up area. To understand the impact of salinity on crops, several vegetation indices (VIs) such as NDVI, SAVI, EVI, and ARVI are used. The LULC changes classified according to VIs are compared with the MOLUSCE plugin based on artificial neural network-multilayer perceptron (ANN-MLP) and Cellular Automata (CA). The comparison of VIs results shows that NDVI is better at describing LULC changes due to the influence of salinity, with a kappa value of 0.63 and a Correctness of 72.565. The LULC projection using CA in all VIs indicates that wetland areas are more likely to convert into water bodies, suggesting that high salinity land tends to be unproductive for rice paddies, making it prone to conversion.

Introduction

Rice fields along the northern coast of Java are experiencing degradation due to various factors such as soil salinity, erosion, and changes in land use [1]. Salinization in coastal paddy fields is driven by topography, climate, parent material of soil, groundwater level, irrigation and drainage conditions, and intrusion of saltwater into the soil as primary factors [2]. These factors contribute to the formation of soil salinization and the migration of water and salt under unsuitable conditions, which negatively impacts crop productivity. The high soil salinity levels in the area, particularly closest to the beach, result in higher sea intrusion [3]. Additionally, changes in climate, such as sea level rise, contribute to salinization of agricultural land near the coast [4]. In addition to these primary factors, secondary factors such as population density and human activity also play a role in the development of soil salinization [5]. Land Use Land Cover (LULC) change, including an increase in settlement areas and a decrease in forest areas, has also had a negative impact on irrigation water supply [6]. Land conversion is another driving force, as the conversion of paddy fields to other uses reduces the availability of suitable land for rice production [7,8]. Salinization can lead to the transformation of different land covers, with saline land having relationships mainly with croplands, grasslands, and water bodies [9].

Remote sensing data of different spatial, temporal, and spectral resolutions obtained from various platforms can be used to monitor the growth and development of crops. Sentinel-2 satellite imagery can be used to monitor the growth phase of rice. Multispectral remote sensing data, including vegetation indices (VIs) and specific salinity indicators derived from Sentinel-2 imagery, are effective in detecting and monitoring soil salinity in rice cultivation fields [10]. The Normalized Difference Vegetation Index (NDVI) value, obtained from

Think twice before printing this journal paper. Save paper, trees, and Earth!

Sentinel-2 imagery, correlates strongly with different stages of rice growth, enabling the rapid identification of growth phases [11]. NDVI has been identified as the most precise index for estimating these phases [12]. Using NDVI values calculated from Sentinel-2 data, paddies affected and unaffected by salinity can be differentiated, with lower NDVI values indicating impaired rice growth [13]. This study utilized Sentinel-2 imagery data to develop a model that estimates the salinity of river water and found that the reflectance of visible bands correlated with Electrical Conductivity (EC), facilitating the monitoring of saline intrusion [14]. Sentinel-2 can also be used to monitor rice-growing conditions over time and identify different patterns of vegetation growth related to soil salinity. This study provides a method for detecting salt-affected soils in irrigated systems [15].

The spatiotemporal changes in the vegetation indices (VIs) from the past to the present, indicating obstacles to plant growth, are likely influenced by plant salinity factors [16,17]. This can serve as a foundation for predicting the impact of salinity on rice paddy agricultural land in the future [18]. The MOLUSCE (Modules for Land Use Change Evaluation) simulation model can assist in understanding the transition from past to present changes, determining the transition probability, and generating future predictions based on detected transition patterns. This study aimed to detect and project changes in LULC spatially and temporally, particularly in detecting the potential impact of salinity from projected changes in coastal rice paddy agricultural land. Sentinel-2 satellite imagery data from 2017, 2019, and 2021 were used in this analysis. The potential impact of salinity on rice paddy fields was identified by comparing VIs such as NDVI, EVI (Enhanced Vegetation Index), ARVI (Atmospherically Resistant Vegetation Index), and SAVI (Soil Adjusted Vegetation Index). A Cellular Automata (CA) model based on MOLUSCE was used as a tool to project future LULC changes up to 2031. Land use and land cover transitions are determined by primary factors driving salinity, such as topography, EC, rivers, and river network density. Additionally, secondary salinity factors mainly influenced by human activities, such as roads, economic centers, and built-up areas, were considered.

Materials and Methods

Study Area

The research site is in the agricultural coastal region of Demak Regency (Figure 1), geographically situated between 6°43'26" and 7°09'43"S, and 110°27'58" and 110°48'47"E. The coastal morphology consists of fluvio-marine plains with slope gradients ranging from to 0 to 8% and elevations between –1 and 10 meter above sea level (masl). This region frequently experiences tidal flooding and coastal erosion due to tidal pattern changes, which are attributed to its lower elevation relative to the sea level and flat terrain. Annual rainfall in Demak averages between 2,000 to 2,500 mm per year. Predominant land use includes rice paddy cultivation, followed by residential areas, industries, fishponds, plantations, and dryland regions.
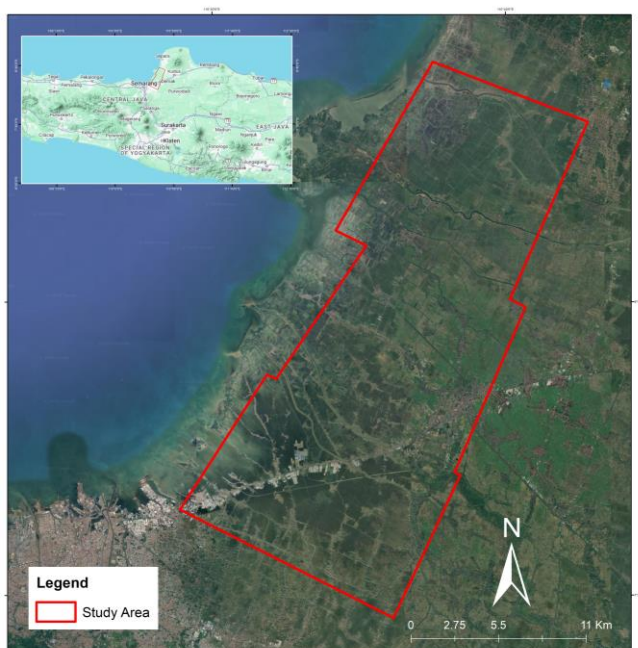

Figure 1. Area Study in Agriculture Coastal Area of Demak Regency.

Data Collection and Preparation

The data source used in the study (Table 1) is the *Rupa Bumi Indonesia* (RBI) or Topographic Map of Indonesia (TMI) provided by the Geospatial Information Agency (GIA), with a scale of 1: 25,000 to obtain information on administrative boundaries, rivers, contours, and land-use layers. Elevation data were detailed using point data from Google to obtain more precise elevation within a 1-meter interval range compared to RBI data with a 12.5-meter interval. Field testing was conducted by collecting soil and water samples for EC parameters through stratified random sampling based on differences in land use and land cover, irrigation channels, rivers, and fishponds. For paddy field polygons, the 2015 Basic Rice Field Map from the Center for Agricultural Data and Information Systems of the Ministry of Agriculture was used.

Table 1. Research data and data sources.

Data	Acquired information	Providers
RBI Map of Demak Regency, Scale 1: 25.000	Geospatial data (River, administrative, LULC)	RBI/GIA
Elevation	Point elevation	Google
Sentinel-2A/B in 2017, 2019 and 2021	VIs (NDVI, EVI, SAVI, ARVI), LULC	Google
Electric Conductivity (EC)	EC	Field survey
paddy field polygons	The boundaries and area of the rice fields.	Ministry of Agriculture

Selection of The Training Area

Sentinel-2 imagery offers high-resolution spatial and temporal data, which is valuable for various environmental monitoring and research applications. Sentinel-2 allows for the detailed observation and analysis of land cover, vegetation health, and water bodies. The spatial resolution varies across different bands: 10 meters for the blue (Band 2), green (Band 3), red (Band 4), and near-infrared (NIR, Band 8). Furthermore, Sentinel-2 provides a temporal resolution of every five days, ensuring frequent and consistent data collection at the same location.

Sentinel-2 image data products were obtained from the Google Earth Engine (GEE) platform between December 2017 and December 2021. The initial stage of image preparation was performed in two stages: geometric correction and radiometric correction. Geometric correction ensures that the spatial positioning of each pixel in the image accurately represents its true location on Earth's surface. This is particularly important for time-series analysis because it allows for accurate comparison of images over time. The GEE platform typically handles geometric corrections automatically, leveraging the internal metadata of Sentinel-2 images that contain precise geolocation information. The second step, radiometric correction, can be expressed with the formula:

$$Reflectance\ corrected = Quantification\ Value \times DN/Solar\ Irradiance \tag{1}$$

where DN is the digital number from the satellite image, and the quantification value is a calibration coefficient provided by Sentinel-2. This correction ensures that the reflectance values accurately represent Earth's surface features.

The planting pattern in Demak Regency was twice a year. However, in this study, the image recording period was chosen to be from April to June with a maximum cloud cover of 30%. In addition, the generative phase was chosen for all three administrative regions; thus, there was a time adjustment, particularly for the Wedung District area. For the Sayung and Bonang Districts, image recording in May was chosen, whereas for the Wedung District, image recording in June was chosen (Table 2).

Table 2. Growth phase conditions of rice recorded by Sentinel-2 for the three administrative regions.

District	2017			2019			2021		
	Apr	May	Jun	Apr	May	Jun	Apr	May	Jun
		19-May	28-Jun		19-May	28-Jun		19-May	28-Jun
Sayung									
Bonang									
Wedung									

Notes: Paddy Phase ▢ Nursery ▢ Vegetative ▢ Generative ▢ Fallow.

Criteria for Land Use and Land Cover

The land use classification obtained from the GIA was further updated through manual interpretation based on Google Earth imagery for 2017, 2019, and 2021. The classification of land use/land cover was divided into six categories: (1) water bodies, including rivers and fish ponds; (2) wetlands, including open land experiencing flooding fluctuations; (3) areas with low vegetation cover, including shrubs and grass, and the seedling phase of rice; (4) areas with medium vegetation cover, including irrigated and non-irrigated rice fields in the vegetative phase; (5) areas with high vegetation cover, including irrigated and non-irrigated rice fields in the generative phase; and (6) built-up areas, including settlements, buildings, roads, and industrial areas. Several appearances of the different phases of rice growth are presented in Figure 2.
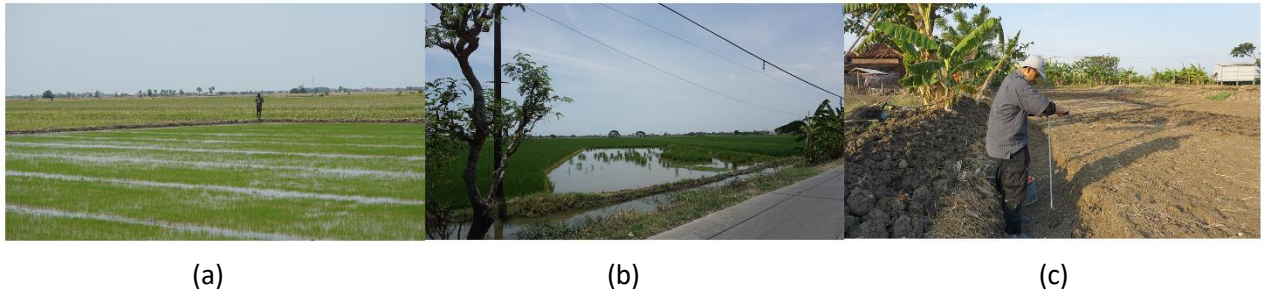

| (a) | (b) | (c) |

Figure 2. Field conditions at different stages of rice development: (a) nursery stage, (b) vegetative stage, and (c) fallow stage. In image (b), differences in rice growth levels can be observed.

Criteria for Vegetation Land Cover by Vegetation Indices (VIs)

The analysis of land cover, particularly in rice paddy fields, through Sentinel-2 involves various VIs such as NDVI, EVI, SAVI, and ARVI (Table 3). These indices are crucial for assessing the health of vegetation by measuring different aspects of plant growth and condition[19,20]. A high NDVI value typically indicates healthy, dense vegetation, whereas lower values may suggest stressed or sparse vegetation, potentially signaling land degradation [21]. EVI, on the other hand, is designed to optimize the vegetation signal in high-biomass regions and improve sensitivity in dense vegetation conditions. It corrects for some of the distortions in the reflected light caused by particles in the air as well as the ground cover below the vegetation. The SAVI was designed to minimize the influence of soil brightness, especially in areas with sparse vegetation. ARVI further improves the NDVI by reducing atmospheric effects.

Table 3. Indirect indicators of salinity using Various VIs.

Index	Name	Description	Equation
NDVI	Normalized Difference Vegetation Index	(NIR-R)/(NIR+R)	(2)
EVI	Enhanced Vegetation Index	2.5(NIR-R)/(NIR+6xR-7.5xB+1)	(3)
SAVI	Soil Adjusted Vegetation Index	[(NIR-R)/(NIR+R+L)](1+L)	(4)
ARVI	Atmospherically Resistant Vegetation Index	[(NIR-(2xR-B)]/[(NIR+(2xR-Blue)]	(5)

Notes: NIR represents the near-infrared band (band 8: wavelength 842 nm), R represents the red band (band 4: wavelength 665 nm), and B represents the blue band (band 2: wavelength 490 nm) of Sentinel-2 imagery, L is the soil brightness correction factor, which is commonly set to 0.5.

VIs values were classified into different vegetation stages using the K-means clustering algorithm. This unsupervised classification method partitions VIs data into K clusters, where K represents a predefined number of clusters. Each data point was iteratively assigned to one of these k clusters based on the mean VIs values of the clusters. The aim is to minimize the variance within each cluster, while maximizing the variance between clusters. As a result, distinct groups of VIs values were formed, corresponding to the different stages of paddy growth.

Field Survey

Soil salinization can be identified by measuring the apparent electrical conductivity (ECa) of the soil [22]. Similarly, the salinity of water can be determined by measuring its electrical conductivity (ECw) [23]. By analyzing the range of ECa and ECw values, it is possible to identify areas with high salinity levels, which indicate salinization [24]. Field testing was conducted in 2021 on 115 water and soil samples (Figure 3) using a stratified random sampling method for each land use and land cover class. Testing and sample area observations were carried out on grids of 100 × 100 m, compositionally representing a 10 × 10-pixel size of

Sentinel-2A/B imagery. The soil EC values were measured using a Hanna HI 98331 Growline Direct Soil Conductivity meter and the water EC values were measured using an Eutech multiparameter water tester. The soil EC values were measured at the root depth of rice plants, which were approximately 0 to 20 cm and 20 to 40 cm deep. Water EC values were measured directly.
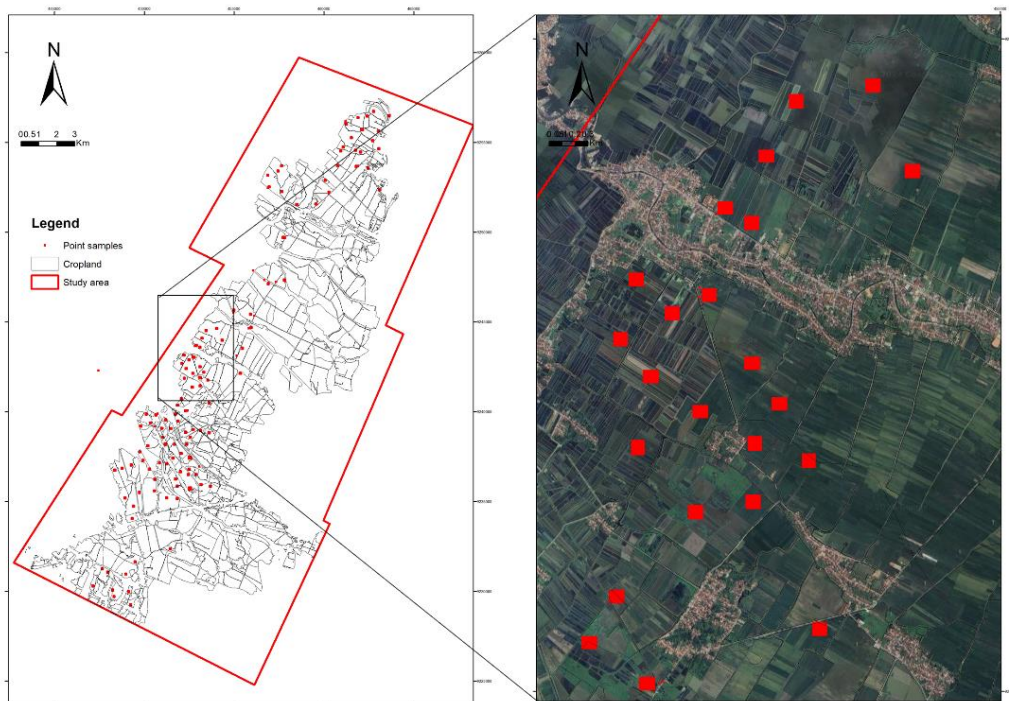

Figure 3. The distribution of the field samples was determined using stratified random sampling within the rice paddy polygons established by Center for Agricultural Data and Information Systems of the Ministry of Agriculture. The sampling grid was set to 100 × 100 m.

Driving Factors

The driving factors of land use and land cover change due to the influence of salinity include the salinity map, topographic map, river density map, distance to the river map, distance to the market map, and distance to built-up area map (Table 4). The Salinity and topography were obtained through kriging interpolation using the QGIS software. The flow density map was obtained using the drainage density plugin in QGIS based on the river layer and a buffer area of 100 m. Euclidean Distance spatial analysis was used to determine the river density map, distance to the river map, distance to the market map, and distance to the built-up area map.

Table 4. Factors driving LULC change influenced by salinity.

Factors	Sources	Analysis
Salinity	EC – field survey	Interpolation krigging
Topography	DEM Google point elevation (1 m)	Interpolation krigging
River density	Line of river and DEM	Geoprocessing tools
Distance from the river	Line of river, RBI	Euclidean distance
Distance from the road	Line of road, RBI	Euclidean distance
Distance from the market	Point of market, RBI- field survey	Euclidean distance
Distance from the building	Area of building, RBI- interpretation	Euclidean distance

Prediction of LU/LC Change

Land use and land cover changes were predicted using the MOLUSCE plugin from the QGIS 2.18 software. This plugin can measure the area of change and predict future LULC using the Artificial Neural Network (ANN) method from CA and Multi-Layer Perceptron (MLP). The formulation of CA is a discrete dynamic system in which the state of each cell at time t + 1 is determined by the state of its neighboring cells at time, according to predefined transition rules. As a method with temporal-spatial dynamics, CA can simulate the evolution of phenomena in two dimensions. CA applies a contiguity filter to 'expand' classifications from historical times

to later periods. MOLUSCE involves six key phases: data input, correlation analysis, area change calculation, potential transition modelling, CA simulation, and validation. Initially, land use and cover data for 2017 and 2019 were input, with each VIs method operating independently. The correlation analysis then examined the factors influencing LULC changes using the Pearson correlation coefficient, removing any factor with a correlation greater than 0.8 to prevent multicollinearity.

Each VIs method uses the same factors. The area change of LULC was calculated by comparing the classifications from 2017 and 2019, with each LULC result running its model. Projections using the MLP algorithm of the ANN estimate the transition potentials with specific settings for neighborhood size, learning rate, maximum iterations, hidden layer size, and momentum. The ANN module outputs maps that show the transition potentials, certainty functions, and simulation outcomes. Changes in LULC for 2021 were simulated using 2017 and 2019 data through the CA algorithm. These predictions were validated against actual 2021 LULC data to verify the model accuracy, employing kappa statistics to assess the precision of the simulation maps. Finally, the number of iterations was adjusted to accommodate a 2-year interval difference, ultimately aiming for a projection that spans 10 years to generate LULC predictions for 2031.

Results and Discussion

Driving Force

The results of the Pearson correlation matrix for the driving factors can be either positive or negative. A positive correlation indicates a linear relationship, where LULC changes coincide with the driving factors, whereas a negative correlation suggests that LULC changes will remain as they were originally. The correlation analysis between the driving factors for LULC changes due to salinity is presented in Table 5.

Table 5. Pearson correlation results for driving factors.

Driving factors	Dist. market	Dist. building	Dist. road	Dist. river	Topographic (krigging)	River density	Salinity (krigging)
Dist. market (X1)		0.2088	0.3112	0.1922	−0.5093	0.1448	0.3023
Dist. building (X2)			0.4366	−0.0453	−0.49	0.2674	−0.0208
Dist. road (X3)				0.6387	−0.3104	−0.1221	−0.0594
Dist. river (X4)					−0.0001	−0.4998	−0.1262
Topographic (krigging) (X5)						−0.4131	−0.1933
River density (X6)							0.0727
Salinity (krigging) (X7)							

Salinity is closely related to the EC values (X7). The EC range in coastal paddy field areas varies and is influenced by several factors. Field test results directly obtained EC values ranging from 2.17 to 4.0 mS/cm (maximum reading value of the device) while laboratory results using the method (ECa) 1:5 obtained a range of 0.15 mS/cm to 1.78 mS/cm. High soil EC was classified with values > 4.0 mS/cm. The amount of fertilizer used affects EC, with interviews with farmers indicating that fields with intensive fertilization have higher EC values than those with less fertilization. High clay content in the subsoil layers of the colluvium and young alluvial plains resulted in higher EC values. EC measurements at soil depths greater than 20 cm also showed high EC values. Overall, the EC range in coastal paddy field areas was influenced by factors such as fertilizer use, measurement depth, spatial variability, and salt accumulation. Water EC is directly measured in drainage flows and rivers. The EC values ranged from 1 to 17.5 mS/cm. High EC values were found near the coastal boundary areas of shrimp ponds and the surrounding agricultural drainage channels. The results for the primary driving factors of salinity are presented in Figure 4, and the secondary driving factors of salinity are shown in Figure 5. Distance to rivers (X4) is one of the variables used in constructing a salinity model, where coastal conditions are very close to the river, indicating a high potential for salinization [25].

The spatial and temporal variability of salinity in coastal delta regions affects subsurface layers and groundwater content, thus becoming a driving factor for salinization [26]. Additionally, the dynamics of estuarine flows impact salinization in aquifers, especially in those with low permeability, compared to high-permeability aquifers. The connection between salinity and topography (X5) is closely associated with processes that cause intrusion and waterlogging on farmlands. Coastal regions characterized by LULC, such as ponds, dunes, barrier islands, and compact drainage systems, are pivotal in the processes of over wash and salinization [27]. Elevations at the study location range from −1.24 masl to 10.52 masl. There is a negative correlation between topographic factors and all other driving factors, suggesting that the potential for land

changes in low-lying or sub-sea level areas often remains unchanged because these areas are typically used for shrimp farming or suffer from seawater flooding. Furthermore, shifts in land use, such as transforming agricultural fields into aquaculture zones, also contribute to the risk of salinity intrusion in coastal regions [28]. Additionally, topography affects the surface qualities of soil and the dynamics of groundwater, which in turn influences the patterns of soil salinization [29]. Prolonged land reclamation in coastal tidal areas can reduce the indicators of soil salinity and improve the accumulation of soil nutrients [30].
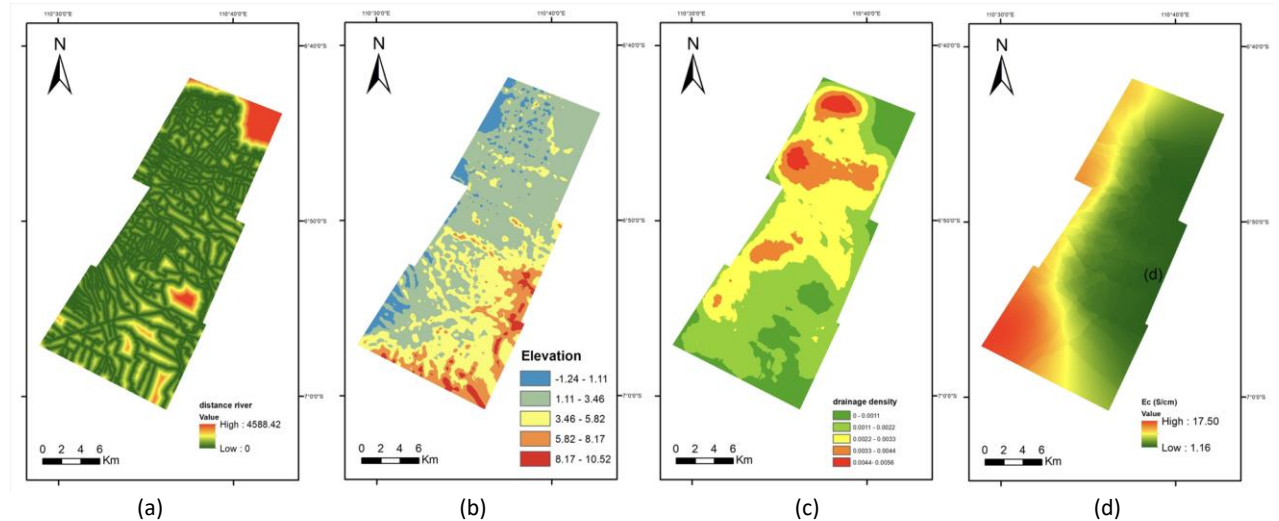

Figure 4. Primary Driving Force to Salinity: (a) Distance to The River (X4); (b) Topography (X5); (c) Drainage Density (X6); (d) Electric Conductivity EC) (X7).
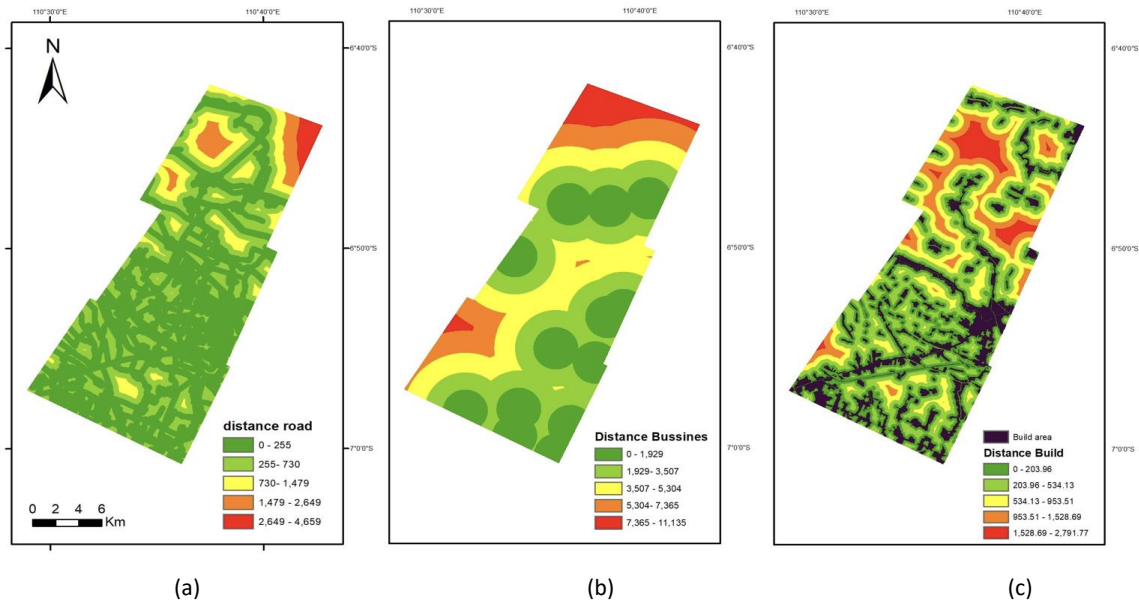

Figure 5. Secondary Driving Force to Salinity: (a) Distance from the Road (X3); (b) Distance from the Market (X1); (c) Distance from the Building (X2).

A high drainage density (X6) plays a significant role in the salinization process, as saline surface water infiltrates the aquifer system [31]. However, the relationship between drainage density and salinization effect occurs through a complex process influenced by various factors, such as irrigation conditions, groundwater salinity, seawater intrusion, climate change, and plant growth. Seawater intrusion/irrigation can threaten biodiversity and crop yields, whereas the leaching of salts from affected areas can increase soil salinity [32].

The secondary factor of distance to the market (X1) positively correlated with the distance to buildings (X2) and the distance to roads (X3). This indicates the relationship between secondary factors and LULC changes, particularly for built-up land use. The relationship between primary and secondary factors driving LULC

changes is shown by a strong positive correlation between the distance to roads (X3) and the distance to rivers (X4), suggesting that areas near infrastructure also tend to be near water sources, potentially supporting the use of land for rice fields. However, a negative correlation between the distance to rivers (X4) and river density (X6) suggests that the farther from the river, the lower the river density, which may indicate a reduced water availability for rice field irrigation.

Transition Matrix of VIs

From the data, we can see the comparison of area extents among VIs (NDVI, EVI, SAVI, and ARVI) from 2017 to 2019 for various parameters, such as water, wetland, low density, moderate density, high density, and building (Table 6). Each index shows different changes for each parameter. For the water parameter, the ARVI index shows the most significant change with an increase of 21.51 km², followed by EVI with an increase of 10.55 km², whereas NDVI only has a slight increase of 0.91 km². For the wetland parameter, ARVI also shows a significant change with an increase of 13.73 km², followed by SAVI with an increase of 11.05 km².

Table 6. Comparison of area extents among VIs for the Years 2017 and 2019.

ID	LULC	NDVI			EVI			SAVI			ARVI		
		2017 (km²)	2019 (km²)	Δ (km²)	2017 (km²)	2019 (km²)	Δ (km²)	2017 (km²)	2019 (km²)	Δ (km²)	2017 (km²)	2019 (km²)	Δ (km²)
1	water	43.09	44	0.91	65.41	75.97	10.55	65.11	73.62	8.51	36.6	57.51	21.51
2	wetland	34.86	42.27	7.41	39.11	47.96	8.85	36.29	47.34	11.05	31.29	45.02	13.73
3	low density	30.54	42.13	11.59	39.93	40.64	0.71	40.46	38.36	−2.1	33.77	37.2	3.43
4	moderat density	49.13	52.98	3.85	95.01	66.89	−28.11	99.26	70.01	−29.25	78.21	47.31	−30.9
5	high density	187.97	154.45	−33.52	106.16	104.05	−2.11	104.49	106.17	1.68	165.72	147.85	−17.8
6	building	57.51	67.26	9.75	57.49	67.61	10.11	57.49	67.61	10.11	57.51	67.61	10.09

For the low-density parameter, the largest change occurred in NDVI with an increase of 11.59 km², while SAVI showed a decrease of 2.1 km². The EVI index showed a small positive change of 0.71 km². For the moderate density parameter, EVI showed the largest change with a decrease of 28.11 km², followed by SAVI with a decrease of 29.25 km². The ARVI experienced the most significant decrease of 30.9 km². From this analysis, it is evident that the ARVI index provides significant changes in several parameters, especially water and wetland, whereas EVI and SAVI show more significant changes in other parameters, such as moderate density. The transition matrix analysis for each VIs (Table 7) and spatially illustrated in Figure 6, shows that ID 1 (water) maintained high stability across all VIs from 2017 to 2019. In the NDVI transition matrix, 85% of the water area remained as water, whereas 15% of the wetland area changed to water. In the EVI transition matrix, the water stability was higher with a value of 92%, with 27% of the wetland area changing to water. The SAVI transition matrix showed water stability at 90%, with 31% of the wetland area changing to water. The ARVI transition matrix showed water stability at 84%, with 50% of the wetland area changing to water.

Table 7. MOLUSCE transition matrix results for each VIs.

		Transition Matrix								Transition Matrix					
		2019								2019					
ID		1	2	3	4	5	6	ID		1	2	3	4	5	6
	1	0.85	0.13	0.01	0.00	0.00	0.00		1	0.92	0.06	0.00	0.00	0.00	0.01
	2	0.15	0.61	0.13	0.02	0.01	0.09		2	0.27	0.43	0.07	0.04	0.06	0.13
2017	3	0.04	0.26	0.41	0.11	0.05	0.13	2017	3	0.06	0.26	0.27	0.17	0.16	0.07
	4	0.01	0.06	0.16	0.30	0.44	0.03		4	0.02	0.08	0.15	0.33	0.42	0.01
	5	0.00	0.02	0.09	0.18	0.70	0.00		5	0.01	0.09	0.12	0.26	0.52	0.01
	6	0.00	0.00	0.00	0.00	0.00	1.00		6	0.00	0.00	0.00	0.00	0.00	1.00
		(a) NDVI								(b) EVI					

		Transition Matrix								Transition Matrix					
		2019								2019					
ID		1	2	3	4	5	6	ID		1	2	3	4	5	6
	1	0.90	0.07	0.01	0.00	0.00	0.02		1	0.84	0.05	0.01	0.00	0.00	0.09
	2	0.31	0.44	0.07	0.02	0.01	0.14		2	0.50	0.30	0.07	0.02	0.02	0.09
2017	3	0.05	0.25	0.24	0.25	0.15	0.06	2017	3	0.18	0.36	0.19	0.10	0.12	0.05
	4	0.01	0.08	0.14	0.33	0.42	0.01		4	0.04	0.11	0.14	0.21	0.49	0.02
	5	0.01	0.08	0.11	0.25	0.55	0.00		5	0.02	0.08	0.11	0.16	0.63	0.00
	6	0.00	0.00	0.00	0.00	0.00	1.00		6	0.00	0.00	0.00	0.00	0.00	1.00
		(c) SAVI								(d) ARVI					

Definition: (1) water; (2) wetland; (3) Low Density (4) Moderat Density (5) High Density (6) Building/Settlement.
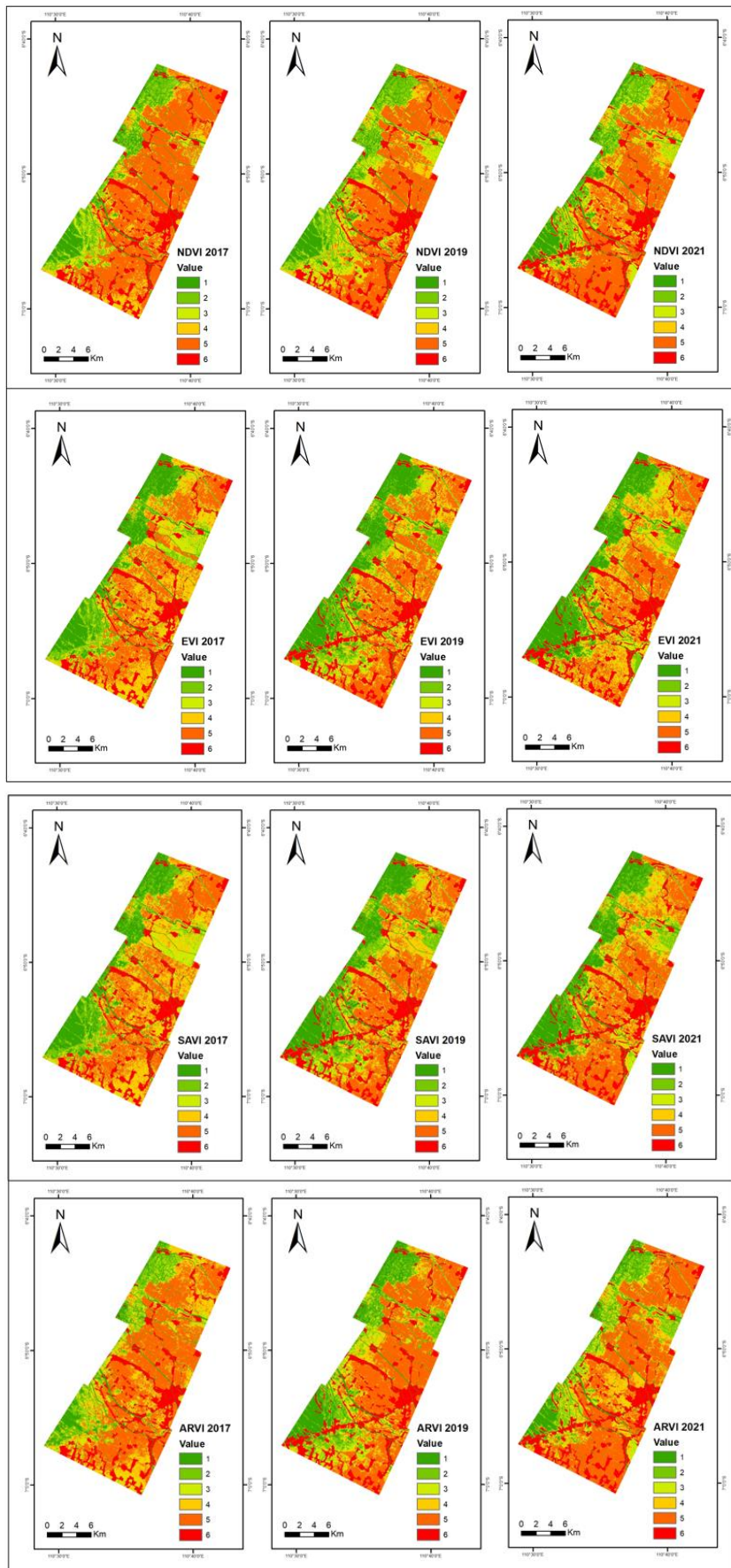
Figure 6. MOLUSCE testing results for each vegetation index (VIs), Definition: (1) water, (2) wetlands, (3) low density, (4) moderate density, (5) high density, and (6) building/settlement.

Additionally, transitions from water to other categories such as low density, moderate density, high density, and buildings are very small or zero across all VIs, indicating that water areas tend not to change to these categories. The smallest transition value recorded from water to other categories was 0.00 in all transition matrices, reinforcing the stability of the water area. This indicates that water is the most stable category and the least likely to change compared to the other categories during the analyzed period. The EVI and ARVI indices showed significant changes from wetland to water, while NDVI and SAVI showed smaller changes.

Validation the Model of LULC NDVI

The MOLUSCE test results for each VIs (NDVI, EVI, SAVI, and ARVI) show various parameters that can be analyzed to determine the most effective VIs (Table 8). Based on the results, NDVI consistently performs the best across most parameters, including Δ Overall Accuracy (−0.00075), Min Validation Overall Error (0.04539), % Correctness (72.565%), Kappa (overall) (0.63617), Kappa (histo) (0.9545), and Kappa (loc) (0.66649). SAVI also showed strong performance in the Current Validation Kappa parameter (0.65653) and had the same minimum validation overall error as NDVI. Consequently, NDVI can be considered the best VIs based on the MOLUSCE test results, followed by SAVI.

Table 8. Results of the MOLUSCE for each tested VIs.

Parameter	NDVI	EVI	SAVI	ARVI
Δ Overall Accuracy	−0.00075	−0.00182	−0.00065	−0.00043
Min Validation Overall Error	0.04539	0.05205	0.04529	0.04915
Current Validation Kappa	0.63345	0.57919	0.65653	0.6226
% Correctness	72.565	62.24	64.4195	60.367
Kappa (overall)	0.63617	0.53662	0.55549	0.478
Kappa (histo)	0.9545	0.83397	0.90521	0.8382
Kappa (loc)	0.66649	0.6434	0.61366	0.5711

Validation the Model of LULC NDVI

The model results were tested from 115 points using the purposive sampling method using desktop observation on-screen with Google Earth and field tests in 2021. A comparison of the NDVI model results and field measurements showed that the overall accuracy for various parameters varied. The water parameter had the highest user accuracy (98%) and producer accuracy (97%), with a kappa coefficient of 0.98, indicating a very high reliability. Meanwhile, low-density vegetation had a lower accuracy, with a user accuracy of 70%, producer accuracy of 60%, and kappa coefficient of 0.65. Moderate-density vegetation showed similar results, while high-density vegetation and wetlands had higher accuracies, with user and producer accuracies of approximately 85% and 80%, respectively.

LULC NDVI Changes (2017, 2019, 2021) and Projection (2031)

The simulation modeling of LULC area changes using MOLUSCE from 2017 to 2031 (Figure 7 and Table 9) reveals significant variations across different LULC categories. The "Water" category shows a slight increase, growing from 43.10 km² in 2017 to 44.01 km² in 2031. Similarly, the "Wetland" category demonstrates a notable increase, expanding from 34.86 km² in 2017 to 42.28 km² in 2031. This suggests a trend toward more water-covered and wetland areas over the 14-year period, potentially due to environmental changes or human activities that favor these types of land cover.

In addition to changes in water and wetland areas, the "Low density vegetation" category also experiences significant growth. It increased from 30.54 km² in 2017 to 42.14 km² in 2031, indicating an increase in areas with sparse vegetation. Meanwhile, "Moderate Density Vegetation" shows a more modest increase from 49.14 km² in 2017 to 52.99 km² in 2031. These increases may be attributed to shifts in agricultural practices, land management strategies, and natural vegetation regrowth. However, the "High Density Vegetation" category, which includes densely forested or heavily vegetated areas, sees a decrease from 187.98 km² in 2017 to 154.46 km² in 2031. This decline highlights the potential loss of dense vegetation areas, possibly owing to land conversion or environmental stressors.

The influence of driving factors such as salinity plays a crucial role in these LULC changes, particularly in the "water" and "wetland" categories. Field observations show that rice fields, when flooded by either seawater intrusion or heavy rainfall, are often converted into fishponds or left submerged. This transformation was a key factor in the observed increase in water and wetland areas. The results of the LULC change projection simulation up to 2031 offer a long-term view of the potential LULC changes.
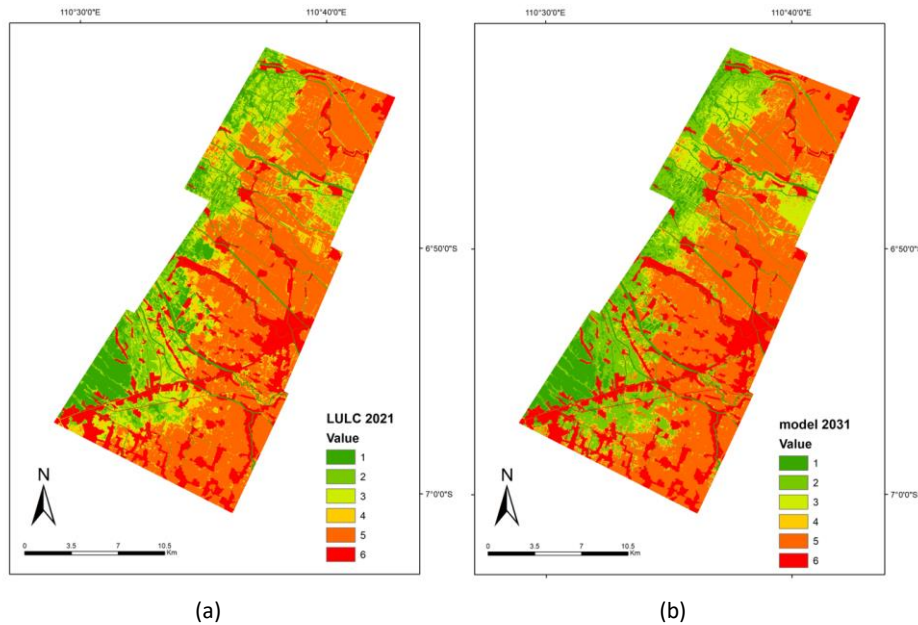
(a)   (b)

Figure 7. Comparison between (a) NDVI 2021 and (b) NDVI 2031 models, Definition; (1) water, (2) wetland, (3) low density, (4) moderate density, (5) high density, (6) building/settlement.

Table 9. The LULC NDVI for the Year 2017, 2019, 2021 and LULC NDVI Projection for the Year 2031.

ID	Land use	2017	2019	2021	2031*	Δ (km²) Year 2017–2031
		km²		
1	Water	43.10	44.01	44.73	44.01	0.91
2	Wetland	34.86	42.28	36.99	42.28	7.41
3	Low density vegetation	30.54	42.14	38.13	42.14	11.60
4	Moderate density vegetation	49.14	52.99	45.25	52.99	3.85
5	High density vegetation	187.98	154.46	170.76	154.46	−33.52
6	Build area	57.52	67.27	67.27	67.27	9.75

Conclusions

This indicates that LULC changes, particularly in paddy agricultural land in the coastal areas of Demak Regency, are influenced by salinity. This can be determined by comparing historical Sentinel LULC data from 2017 and 2019 in detail with the VIs classification (NDVI, EVI, SAVI, and ARVI). The Pearson correlation results showed that the primary salinity driving factors were distance to the river and topography. Secondary factor variables are influenced by the distance to the road. The ANN-MLP projection of each VIs was then classified into six LULC classifications, namely water, wetland, low-density, moderate-density, high-density, and building, showing a decrease around moderate-to-high-density vegetation land cover classification to non-agricultural LULC (water, wetland, building, or low-density vegetation areas). The reliability of LULC projections for each VIs uses MOLUSCE based on CA. NDVI can be considered as the best VIs based on the MOLUSCE test results. The LULC model validation results of NDVI showed that the parameters of water, high-density vegetation, and wetlands had high accuracy. The low-density vegetation had the lowest accuracy. The projection until 2031 showed a slight increase in the water classification LULC and a significant increase in wetland classification. Among the vegetation classifications, a significant decrease was observed in high-density vegetation classification.

Author Contributions

TAT: Conceptualization, Methodology, Software, Investigation, Writing - Review & Editing; **BB, MYJ, SA, WW**: Supervision, Review.

Conflicts of interest

There are no conflicts to declare.

References

1. Tarigan, S.D.; Tukayo, R.K. Impact of Land Use Change and Land Management on Irrigation Water Supply in Northern Java Coast. *J. Trop. Soils* **2013**, *18*, 169–176, doi:10.5400/JTS.2013.V18I2.169-176.

2. Li, J.; Yang, W.; Wang, Y.; Li, Q.; Liu, L.; Zhang, Z. Carbon Footprint and Driving Forces of Saline Agriculture in Coastally Reclaimed Areas of Eastern China: A Survey of Four Staple Crops. *Sustainability* **2018**, *10*, 1–16, doi:10.3390/SU10040928.

3. Hikmat, M.; Yatno, E.; Suryani, E. Salinity of Paddy Field in Main Landforms in Indramayu Regency, West Java. *IOP Conf. Ser. Earth Environ. Sci.* **2021**, *648*, 12036, doi:10.1088/1755-1315/648/1/012036.

4. Daris, E.; Aminudin, I.; Feriansyah, A. Determinants of Paddy Fields Conversion in Java Island, Indonesia. *Advances in Intelligent Systems Research (AISR)* **2018**, *149*, 95–98.

5. Jian-ron, C. Analysis for Driving Forces and Ecological Risk Assessment of Soil Salinization in the Yellow River Delta. *Adv. Mar. Sci.* **2014**, *32*, 508–516.

6. Shukla, S.P.; Meshesha, T.W.; Sen, I.S.; Bol, R.; Bogena, H.; Wang, J. Assessing Impacts of Land Use and Land Cover (LULC) Change on Stream Flow and Runoff in Rur Basin, Germany. *Sustainability* **2023**, *15*, 1–24, doi:10.3390/su15129811.

7. Adnan, A.M.I. Farmers' Perspective on Converting Their Paddy Fields in West Java Province. *Agriekonomika* **2023**, *12*, 48–67, doi:10.21107/agriekonomika.v12i1.16589.

8. Karolinoerita, V.; Annisa, W. Salinisasi Lahan Dan Permasalahannya Di Indonesia. *J. Sumberd. Lahan* **2020**, *14*, 91–99, doi:10.21082/JSDL.V14N2.2020.91-99.

9. Duan, S.; Kaushal, S.S. Salinization Alters Fluxes of Bioreactive Elements from Stream Ecosystems across Land Use. *Biogeosciences* **2015**, *12*, 7331–7347, doi:10.5194/BG-12-7331-2015.

10. Gerardo, R.; de Lima, I.P. Sentinel-2 Satellite Imagery-Based Assessment of Soil Salinity in Irrigated Rice Fields in Portugal. *Agriculture* **2022**, *12*, 1–20, doi:10.3390/agriculture12091490.

11. Novitasari, N. Relationship Between Normalized Difference Vegetation Index (NDVI) and Rice Growth Phases in Danda Jaya Swamp Irrigation Area Regency Barito Kuala. *IOP Conf. Ser.* **2023**, *1184*, 12019, doi:10.1088/1755-1315/1184/1/012019.

12. Hisham, N.H.B.; Hashim, N.I.; Saraf, N.M.; Talib, N. Monitoring of Rice Growth Phases Using Multi-Temporal Sentinel-2 Satellite Image. *IOP Conf. Ser. Earth Environ. Sci.* **2022**, *1051*, 12021, doi:10.1088/1755-1315/1051/1/012021.

13. Tivianton, T.A.; Barus, B.; Purwanto, M.Y.J.; Anwar, S.; Widiatmaka; Laudiansyah, R. Temporal NDVI Analysis to Detect the Effects of Seawater Intrusion on Rice Growth in Coastal Areas. *IOP Conf. Ser. Earth Environ. Sci.* **2021**, *662*, 12021, doi:10.1088/1755-1315/662/1/012021.

14. Sakai, T.; Omori, K.; Oo, A.N.; Zaw, Y.N. Monitoring Saline Intrusion in the Ayeyarwady Delta, Myanmar, Using Data from the Sentinel-2 Satellite Mission. *Paddy Water Environ.* **2021**, *19*, 1–12, doi:10.1007/S10333-020-00837-0.

15. Moussa, I.; Walter, C.; Michot, D.; Boukary, I.A.; Nicolas, H.; Pichelin, P.; Guero, Y. Soil Salinity Assessment in Irrigated Paddy Fields of the Niger Valley Using a Four-Year Time Series of Sentinel-2 Satellite Images. *Remote Sens.* **2020**, *12*, 1–17, doi:10.3390/RS12203399.

16. Huo, D. Mapping Soil Salinity Using a Combination of Vegetation Index Time Series and Single-Temporal Remote Sensing Images in the Yellow River Delta, China. *Catena* **2023**, *231*, 107313, doi:10.1016/j.catena.2023.107313.

17. Han, Y.; Lin, Y.; Zhou, P.; Cao, Z. Dynamic Change, Driving Mechanism and Spatiotemporal Prediction of the Normalized Vegetation Index: A Case Study from Yunnan Province, China. *Front. Ecol. Evol.* **2023**, *11*, 1177849, doi:10.3389/fevo.2023.1177849.

18. Kalambukattu, J.G.; Johns, B.; Kumar, S.; Raj, A.D.; Ellur, R.S. Temporal Remote Sensing Based Soil Salinity Mapping in Indo-Gangetic Plain Employing Machine-Learning Techniques. *Proc. Indian Natl. Sci. Acad.* **2023**, *89*, 1–16, doi:10.1007/s43538-023-00157-x.

19. Tian, J.; Tian, Y.-Z.; Liu, K. Research on Rice Fields Extraction by NDVI Difference Method Based on Sentinel Data. *Sensors* **2023**, *23*, 1–16, doi:10.3390/s23135876.

20. Eguchi, T.; Tasumi, M. Paddy Rice Double-Cropping Field Monitoring via Vegetation Indices with Limited Ground Data—A Case Study for Thapanzeik Dam Irrigation District in Myanmar. *Agriculture* **2023**, *13*, 1–13, doi:10.3390/agriculture13040851.

21. Kaligis, D.A.; Manggau, F.X. Health Analysis of Rice Plants Based on the Normalized Difference Vegetation Index (Ndvi) Value in Image of Unmanned Aircraft (Case Study of Merauke - Papua Selatan). *Eng. Technol. J.* **2023**, *08*, 1986–1991, doi:10.47191/etj/v8i2.04.

22. Buta, M.; Paulette, L.; Man, T.; Bartha, I.; Negrusier, C.; Bordea, C. Spatial Assessment of Soil Salinity by Electromagnetic Induction Survey. *Environ. Eng. Manag. J.* **2019**, *18*, 2073–2081, doi:10.30638/EEMJ.2019.197.

23. Cassel, F.; Goorahoo, D.; Sharmasarkar, S. Salinization and Yield Potential of a Salt-Laden Californian Soil: An In Situ Geophysical Analysis. *Water Air Soil Pollut.* **2015**, *226*, 422, doi:10.1007/S11270-015-2682-1.

24. Louati, D.; Majdoub, R.; Rigane, H.; Abida, H. Effects of Irrigating with Saline Water on Soil Salinization (Eastern Tunisia). *Arab. J. Sci. Eng.* **2018**, *43*, 3793–3805, doi:10.1007/S13369-018-3215-1.

25. Thiam, S.; Villamor, G.B.; Faye, L.C.; Sène, J.H.B. Monitoring Land Use and Soil Salinity Changes in Coastal Landscape: A Case Study from Senegal. *Environ. Monit. Assess.* **2021**, *193*, 1–18, doi:10.1007/S10661-021-08958-7.

26. Song, Y.; Gao, M.; Wang, Z.; Gong, T.F.; Chen, W. Spatio–Temporal Variability Characteristics of Coastal Soil Salinization and Its Driving Factors Detection. *Water* **2022**, *14*, 1–17, doi:10.3390/w14203326.

27. Yu, X.; Yang, J.; Graf, T.; Koneshloo, M.; O'Neal, M.A.; Michael, H.A. Impact of Topography on Groundwater Salinization Due to Ocean Surge Inundation. *Water Resour. Res.* **2016**, *52*, 5794–5812, doi:10.1002/2016WR018814.

28. Hasan, M.H.; Hossain, M.J.; Chowdhury, M.A.; Billah, M. Salinity Intrusion in Southwest Coastal Bangladesh: An Insight from Land Use Change. In *Water, Flood Management and Water Security Under A Changing Climate*; Haque, A., Chowdhury, A., Eds.; Springer: Cham, 2020.

29. Celleri, C. Spatial and Temporal Patterns of Soil Salinization in Shallow Groundwater Environments of the Bahía Blanca Estuary: Influence of Topography and Land Use. *L. Degrad. Dev.* **2022**, *33*, 470–483, doi:10.1002/ldr.4162.

30. Xie, X.; Pu, L.; Zhu, M.; Xu, Y.; Wang, X. Linkage between Soil Salinization Indicators and Physicochemical Properties in a Long-Term Intensive Agricultural Coastal Reclamation Area, Eastern China. *J. Soils Sediments* **2019**, *19*, 3699–3707, doi:10.1007/S11368-019-02333-3.

31. Giambastiani, B.M.S.; Macciocca, V.R.; Molducci, M.; Antonellini, M. Factors Affecting Water Drainage Long-Time Series in the Salinized Low-Lying Coastal Area of Ravenna (Italy). *Water* **2020**, *12*, 1–23, doi:10.3390/W12010256.

32. Pereira, C.S.; Lopes, I.; Abrantes, I.; Sousa, J.P.; Chelinho, S. Salinization Effects on Coastal Ecosystems: A Terrestrial Model Ecosystem Approach. *Philos. Trans. R. Soc. B* **2019**, *374*, 20180251, doi:10.1098/RSTB.2018.0251.